Asian Journal of Pharmaceutical Sciences 17 (2022) 412–424

Available online at www.sciencedirect.com

ScienceDirect

journal homepage: www.elsevier.com/locate/AJPS

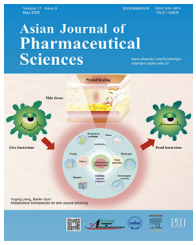

Original Research Paper

Elaborately engineering of a dual-drug co-assembled nanomedicine for boosting immunogenic cell death and enhancing triple negative breast cancer treatment

Chen Wang[#], *Han Yu*[#], *Xiaohong Yang, Xuanbo Zhang, Yuequan Wang, Tianrui Gu, Shenwu Zhang*[*], *Cong Luo*[*]

Shenyang Pharmaceutical University, Shenyang 110016, China

ARTICLE INFO

Article history:
Received 22 December 2021
Revised 11 February 2022
Accepted 23 February 2022
Available online 3 March 2022

Keywords:
Carrier-free
Pure drug co-assembly
Immune activation
Synergistic chemo-photothermal therapy

ABSTRACT

Pure drug-assembled nanosystem provides a facile and promising solution for simple manufacturing of nanodrugs, whereas a lack of understanding of the underlying assembly mechanism and the inefficient and uncontrollable drug release still limits the development and application of this technology. Here, a simple and practical nanoassembly of DOX and DiR is constructed on basis of their co-assembly characteristics. Multiple interaction forces are found to drive the co-assembly process. Moreover, DOX release from the nanoassembly can be well controlled by the acidic tumor microenvironment and laser irradiation, resulting in favorable delivery efficiency of DiR and DOX *in vitro* and *in vivo*. As expected, the nanoassembly with high therapeutic safety completely eradicated the mice triple negative breast cancer cells (4T1) on BALB/c mice, owing to synergistic chemo-photothermal therapy. More interestingly, DiR and DOX synergistically induce immunogenic cell death (ICD) of tumor cells after treatment, enabling the mice to acquire immune memory against tumor growth and recurrence. Such a facile nanoassembly technique provides a novel multimodal cancer treatment platform of chemotherapy/phototherapy/immunotherapy.

1. Introduction

Small-molecule drugs still play important roles in cancer therapy [1–3]. However, some distinct drawbacks still restrict their therapeutic effect, such as poor water solubility, fast clearance from the blood circulation, lack of tumor targeting, as well as acquired drug resistance [4–6]. A wide range of nano drug delivery systems (NDDSs) have been developed for anticancer drug delivery, such as liposomes and micelles [7–9]. There's no denying that encapsulation of small-molecule drugs into nanocarriers can effectively improve their inferior properties and facilitate therapeutic outcomes [10]. Nevertheless, the clinical translation of NDDSs still faces

* Corresponding authors.
E-mail addresses: zhangshenwu@aliyun.com (S.W. Zhang), luocong@syphu.edu.cn (C. Luo).
# These authors contributed equally to this work.
Peer review under responsibility of Shenyang Pharmaceutical University.

https://doi.org/10.1016/j.ajps.2022.02.004

numerous challenges, mainly including complex preparation processes, low drug loading efficiency, and ingredient-induced toxicity [11–13].

Recently, a new style of NDDSs assembled by pure drug molecules has aroused great interest in the biomedical field [14–17]. The formulation of pure drug-assembled nanosystem (PDANS) is mainly driven by the supramolecular interactions, such as hydrophobic interactions, hydrogen bond interactions, and metal-coordination interactions between drug molecules [15,18]. PDANS represents a landmark nanomedicine, which is no longer dependent on carrier materials. In other words, drug molecules themselves can spontaneously assemble into uniform nanoparticles (NPs) in water [19,20]. For this reason, PDANS is also known as self-delivering nanomedicine. Notably, PDANS can reduce even avoid the potential toxic side effects caused by the heavy use of carrier materials. More importantly, PDANS is usually fabricated by the one-step nano-precipitation method [21,22]. The preparation technique is pretty simple and convenient with good reproducibility, which is conducive to industrial manufacture and clinical translation [15]. At present, the pure drug nanoassembly technique has been applied to facilitate the efficient delivery of chemotherapeutic drugs [2], photosensitizers [18,23], as well as immunotherapy drugs [24]. Moreover, there have been nanodrugs based on pure drug nanoassembly techniques entering clinical trials [25].

In addition, since cancer is a systemic disease [10,26], focusing merely on tumor growth inhibition might not be enough to fundamentally achieve a good therapeutic effect [13,27,28]. A large number of clinical data showed that although the tumors of many patients could be almost completely removed from the body in the short term, the high risk of tumor recurrence eventually led to treatment failure [29]. Therefore, it is necessary to train the immune system in the course of treatment for systemic long-term protection [6,30]. An increasing body of evidence suggests that some therapeutic strategies exhibit immune-modulating effects, such as chemotherapy and phototherapy, which could produce damage-associated molecular patterns (DAMPs) to activate the immune system [31,32]. Therefore, the effects of traditional treatments on the immune system have received more and more attention, which bridge the gap between traditional cancer treatments and immunotherapy.

Recently, photothermal therapy (PTT) has emerged as a noninvasive and reliable cancer-therapy modality, which could rapidly increase the temperature of tumor cells and further ablate the tumors by activating photosensitizer and producing thermal energy under the near-infrared (NIR) light irradiation [33–35]. Moreover, studies have shown that phototherapy including photodynamic therapy (PDT) and PTT can also induce immunogenic cell death (ICD) and activate the immune response during apoptosis [36]. Briefly, PTT not only kills cancer cells by producing local hyperthermia but also triggers indirectly endoplasmic reticulum pressure resulting in the release of DAMPs [37]. The released DAMPs were presented by antigen-presenting cells (APCs) to stimulate the maturation of dendritic cells (DCs) and further activate the effector T cells. Therefore, the ICD-based immunotherapy induced by PTT can efficiently cooperate with PTT to achieve comprehensive suppression both of primary and metastatic tumors.

Herein, we report a novel hybrid PDANS co-assembled by DOX and DiR (Fig. 1). We found that both DOX and DiR could self-assemble into uniform NPs in water. Interestingly, they could also form stable co-assemblies at multiple molar ratios, offering the opportunity for precision combination cancer therapy. The hydrophobic and π-π stacking interactions were found to be the main driving factors of the assembly, which were analyzed by molecular docking simulation technique and verified by interaction-breaking experiments. Surprisingly, DOX release from the co-assembled system was found to intelligently respond to acidic tumor environment and laser irradiation, significantly reducing its systemic toxicity [38]. After PEG modification, the co-assembled NPs could significantly extend the systemic circulation time and increase the accumulation in tumor tissues. As expected, the tumors were almost eliminated after synergetic chemo-photothermal therapy. Surprisingly, the nanoassembly effectively boosted immune response and inhibited tumor recurrence by establishing long-term immune memory (Fig. 1). Such a pure drug molecular co-assembly nanosystem provides a promising platform for small-molecule drug-based chemo-photo-immunotherapy.

2. Materials and methods

2.1. Materials

DiR, DOX, and cell culture media were obtained from Meilun Biotech Co. Ltd. DSPE-PEG_{2K} were obtained from A.V.T. (Shanghai) Pharmaceutical Co., Ltd. Anti-CD62L (APC), anti-CD44 (PE), anti-CD86 (APC), anti-CD80 (PE), anti-CD11c (FITC), anti-CD3 (PerCP-Cy5.5), anti-CD4 (PE), anti-CD8 (FITC) were acquired from BioLegend, Inc (USA). The lymphocyte separation liquid was provided by Beijing Solarbio Science & Technology Co., Ltd, China. Other reagents used in this study were of the analytical grades.

2.2. NPs preparation and characterization

To make self-assembled DiR or DOX NPs, ethanol containing 5 mg/mL DiR or DMSO containing 5 mg/mL DOX were dropped in water under vigorous stirring. To make co-assembled DiR-DOX NPs, DiR and DOX were dissolved in the mixed solution of ethanol and DMSO (2:1, *v*/*v*), and dropped in stirred water. Organic solutions were removed by ultrafiltration. For PEG decoration, DSPE-PEG_{2K} dissolved in ethanol was added to the prepared NPs. The particle size and morphology were respectively acquired by a Zetasizer (Nano ZS, Malvern Co.) and transmission electron microscope (Hitachi, HT7700). The microparticles of DiR-DOX NPs were prepared by dropping the mixed organic solution of 20 mg/mL DiR and 5.4 mg/mL DOX in a gently stirred PBS. DOX Sol, DiR Sol and DiR-DOX-PEG NPs at an equivalent DOX concentration or DiR concentration were added into the 96-well plates, and then fluorescence spectra or UV spectra were then acquired by a microplate reader. To make the lyophilized sample, DiR-DOX-

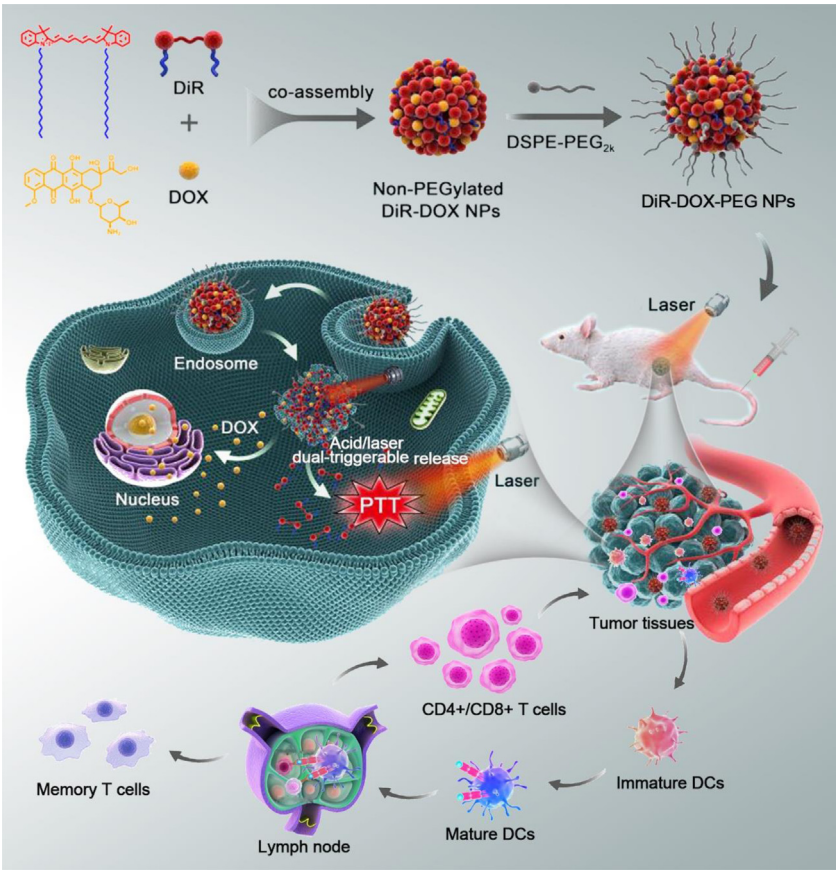

Fig. 1 – Schematic illustration of the co-assembled nanosystem of DiR and DOX for immune-activating chemo-photo-immunotherapy.

PEG NPs were dissolved with 7% sucrose and processed with a universal lyophilization program.

2.3. *Molecular docking*

Molecular docking results were acquired by uploading the chemical structure to Yinfo Cloud Platform and automatically analyzed.

2.4. *Stability in different media*

The *in vitro* stability of DiR-DOX NPs and DiR-DOX-PEG NPs was tested in RPMI-1640 media containing FBS (10%, *v/v*). The stability of the NPs in different media (NaCl, urea, sodium dodecyl sulfate) for different incubation periods was evaluated by monitoring the hydrodynamic diameter by DLS.

2.5. *In vitro photothermal effect and drug release*

To evaluate the photothermal effect, different concentrations of DiR-DOX-PEG NPs were irradiated with an 808 nm laser (3 W/cm^2, 3 min). The temperature changes were recorded by a thermal imaging instrument (Fotric 226). *In vitro* release profiles of DOX from co-assembled NPs were determined by adding 200 µl formulation (with/without irradiation, 3 W/cm^2, 5 min) into a dialysis tube (molecular weight cut-off of 10 kDa) and immersed into 30 mL PBS (pH 7.4, 6.8 and 5.0). At predetermined time intervals, the release amount of DOX was measured by a microplate reader.

2.6. *Cell culture*

Mice triple negative breast cancer cells (4T1) were cultured in RPMI 1640 medium (containing penicillin/streptomycin) with 10% fetal bovine serum (FBS).

2.7. *In vitro cellular uptake*

1.2×10^6 4T1 cells were seeded in 12 well plates and incubated for 12 h. DiR Sol, DiR-DOX NPs, and DiR-DOX-PEG NPs (containing 2 µg/ml of DiR) were then incubated with cells for 0.5 and 2 h. After washing and fixing, the cells were observed by confocal laser scanning microscopy (Nikon, C2 Plus) or analyzed by flow cytometer (BD, FACSCalibur).

2.8. *Cytotoxicity*

4T1 cells were seeded in 96-well plates (3.0×10^3 cells per well). After culturing for 24 h, the cells were treated with DOX Sol, DiR-DOX NPs, or DiR-DOX-PEG NPs (with or without laser irradiation for 5 min, 3 W/cm^2, 4 h after incubation). The DiR or DOX concentrations in NPs were equivalent to that of the

free solution. 24 h after the treatment, the cell viability was detected using MTT.

2.9. Penetration of DiR-DOX-PEG NPs in cell spheroids

Cell spheroids were established according to previous work [16]. To evaluate the penetration effect, DOX Sol and DiR-DOX-PEG NPs were incubated with the cell spheroids for 4 h. At 2 h of incubation, the cell spheroids were irradiated with 808 nm laser (3 W/cm^2, 5 min) and then keep incubated. The confocal images were taken after 4 h incubation.

2.10. Biomarkers of DiR-DOX-PEG NPs induced ICD

To determine and quantify the ICD effect of DiR-DOX-PEG NPs treatment, 4T1 cells were seeded in 24 well plates and treated with the same condition in cytotoxicity under a concentration of IC50 value. 12 h after the treatment, the cells and culture medium were collected for analysis. To observe the distribution of calreticulin (CRT) and HMGB1, cells were cultured on glass slides in 24 well plates. After the treatment, cells were fixed and permeabilized with Triton (for HMGB1 observation), washed and incubated with primary antibodies and FITC conjugated secondary antibodies respectively. To quantify CRT and HMGB1, cells after antibodies stain were collected and analyzed by flow cytometer. To analyze the ATP secretion, the collected culture medium was tested by an ATP assay kit.

2.11. Bone marrow-derived dendritic cells (BMDCs) maturation stimulated by ICD

BMDCs were collected from the bone marrow of mice and cultured with IL-4 and granulocyte macrophage colony stimulating factor. After 5 d of culture, the DCs were incubated with 4T1 cells under different treatments for 12 h. Then the DCs were collected and stained with anti-CD86 (APC), anti-CD80 (PE), and anti-CD11c (FITC) for qualitative analysis by flow cytometer.

2.12. Animals

The use of animals is approved by the Animal Ethics Committee of Shenyang Pharmaceutical University (No. 16,178). BALB/c mice and SD rats were provided from the Experimental Animal Center of Shenyang Pharmaceutical University.

2.13. Pharmacokinetics

SD rats (180–200 g) were *i.v.* injected with DiR Sol, DOX Sol, DiR-DOX NPs, and DiR-DOX-PEG NPs (5 mg/kg of DiR, 1.3 mg/kg of DOX). The plasma was collected at predesigned time points and measured according to the previous method [18].

2.14. Biodistribution

The *in vivo* and *ex vivo* distribution were investigated by 4T1 tumor-bearing mice established by subcutaneous injection of 5×10^6 cells. When the tumor volume reached 300–400 mm^3, the mice were firstly *i.v.* injected with DiR Sol, DiR-DOX NPs, and DiR-DOX-PEG NPs (1 mg/kg of DiR). At 1, 2, 4, 12, and 24 h, DiR fluorescence was monitored by the Caliper IVIS Lumina II. Another group of mice was reinjected and sacrificed at their maximum accumulation for *ex vivo* distribution analysis.

2.15. In vivo photothermal effects

The tumor-bearing mice (weight: 18–22 g; tumor volume: 300–400 mm^3) were firstly *i.v.* injected with saline, DiR Sol, DiR-DOX NPs, and DiR-DOX-PEG NPs (1 mg/kg of DiR), respectively. At 4 h (DiR Sol) or 12 h (DiR-DOX NPs and DiR-DOX-PEG NPs), the mice were anesthetized and the tumor sites were exposed to the laser (2.0 W/cm^2) for 5 min. The temperature changes were monitored using a thermal infrared imaging camera (Fortic 226) simultaneously.

2.16. In vivo anticancer effects

Thirty 4T1 tumor-bearing mice (weight: 18–22 g, tumor volumes were around 100 mm^3) were randomly divided into six groups and separately injected with Saline, DiR Sol, DOX Sol, DiR-DOX NPs, and DiR-DOX-PEG NPs for each group (DiR: 5.0 mg/kg, DOX: 1.35 mg/kg). After 4 or 12 h, DiR Sol, DiR-DOX NPs, and DiR-DOX-PEG NPs were irradiated with an 808 nm laser (2.0 W/cm^2, 5 min) for PTT. The mice were treated every two days. After five treatments, the mice were killed, and the main organs, as well as tumors and serum samples, were collected and analyzed.

2.17. Tumor recurrence prevention

To evaluate the tumor recurrence prevention of DiR-DOX-PEG NPs, the first tumor was inoculated in the left flank of mice and then treated with DiR-DOX-PEG NPs or saline as described in the *in vivo* anticancer effect. Ten days after the first tumor was eliminated or removed by surgery, the second tumor was inoculated at the right flank of mice. The size of the second tumor was recorded every other day until the mice were sacrificed.

2.18. Western blot analysis of CRT in tumors

To analyze CRT in tumors, 4T1 tumor-bearing mice were killed after three times of treatment of DiR-DOX-PEG NPs. The tumors were collected and grinded. The proteins were extracted processed as previously described [39].

2.19. In vivo lymphocytes analysis

To analyze DCs maturation *in vivo*, after the treatment, the inguinal LNs of half of the mice were collected. DCs were separated and stained with anti-CD86 (APC), anti-CD80 (PE), and anti-CD11c (FITC) before being examined by flow cytometric measurement. To examine the T lymphocytes in peripheral blood, the blood of mice was collected and mononuclear cells were isolated by lymphocyte separation medium. The lymphocytes were stained with anti-CD3 (PerCP-Cy5.5), anti-CD4 (PE), anti-CD8 (FITC). To analyze memory T lymphocytes, the spleens of the surviving mice were collected

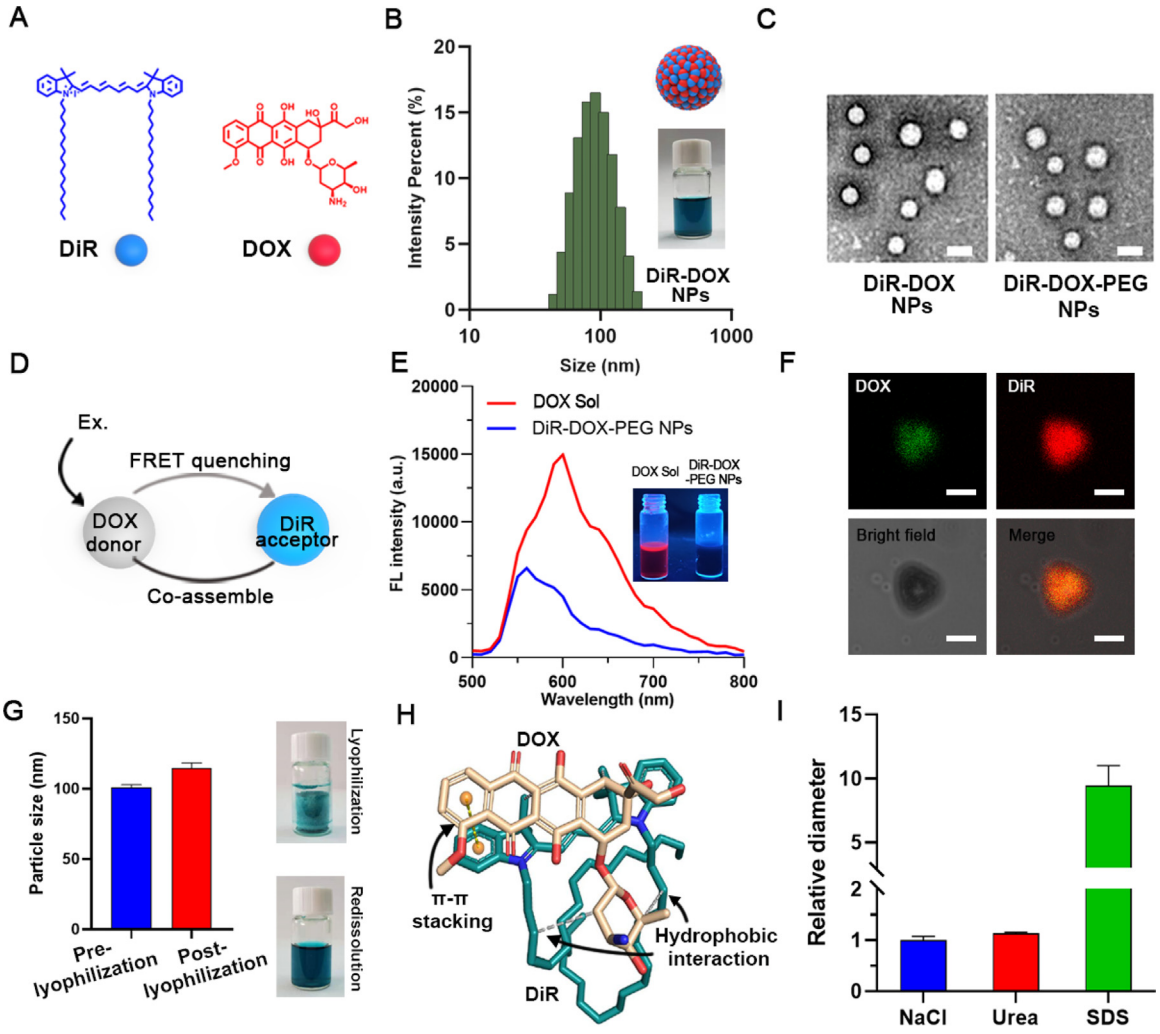

Fig. 2 – Co-assembly of DOX and DiR. (A) Molecule structure of DOX and DiR. (B) DLS results of DiR-DOX NPs at a concentration of 1 mg/mL. (C) TEM images of DiR-DOX NPs and DiR-DOX-PEG NPs. (Scale bar represents 100 nm) (D) Schematic of the FRET-quenching of DOX in DiR-DOX-PEG NPs. (E) Fluorescence spectrum of DOX Sol and DiR-DOX-PEG NPs (*Ex*: 300 nm). Photographs show the DOX Sol and DiR-DOX-PEG NPs under UV light at 365 nm. (F) Confocal images of a microsized particle of DiR-DOX with different channels (scale bar represents 5 μm). (G) Diameters and represent figures of DiR-DOX-PEG NPs pre- and post- lyophilization. (H) Molecular docking result of DiR (yellow) and DOX (cyan) (The gray dotted line represents hydrophobic interaction force, and the yellow dotted line represents π-π stacking force). (I) Relative diameter of DiR-DOX-PEG NPs in different buffer solutions.

30 d post-treatment. Tissues were treated by grinding. The cell suspension was stained with anti-CD8 (FITC), anti-CD62L (PE), and anti-CD44 (APC).

2.20. *Statistical analysis*

The results are presented as mean ± SD. One-way ANOVA analysis and *t*-test were used to analyze data from different groups. $P < 0.05$ is considered significant.

3. Results and discussion

3.1. *Co-assembly of DOX and DiR*

In our previous work, we found that DiR could readily assemble into NPs. Given that the desalted doxorubicin (DOX) is also a hydrophobic molecule with aromatic groups (Fig. 2A), it might also have the self-assembly capacity. As shown in Fig. S1, both DiR and DOX demonstrated good assembly capability in water. Furthermore, we further explored the co-assembly capacity of the two drugs for combination cancer therapy. Interestingly, DOX and DiR could also form co-assembled NPs (DiR-DOX NPs) with a diameter range from 60 to 90 nm at various molar ratios (Fig. 2B, Table S1). An optimal molar ratio of 2:1 (DiR: DOX) was then chosen by synergistic effect screening of 4T1 tumor cells (Table S2). A small amount of DSPE-PEG_{2K} was used to fabricate the PEGylated DiR-DOX NPs (DiR-DOX-PEG NPs). TEM results showed that DiR-DOX NPs and DiR-DOX-PEG NPs had a uniform spherical shape with average diameters of ~80 nm (Fig. 2C). To confirm whether DiR and DOX were co-assembled into hybrid NPs, the fluorescence spectra of DOX NPs and DiR-DOX NPs were

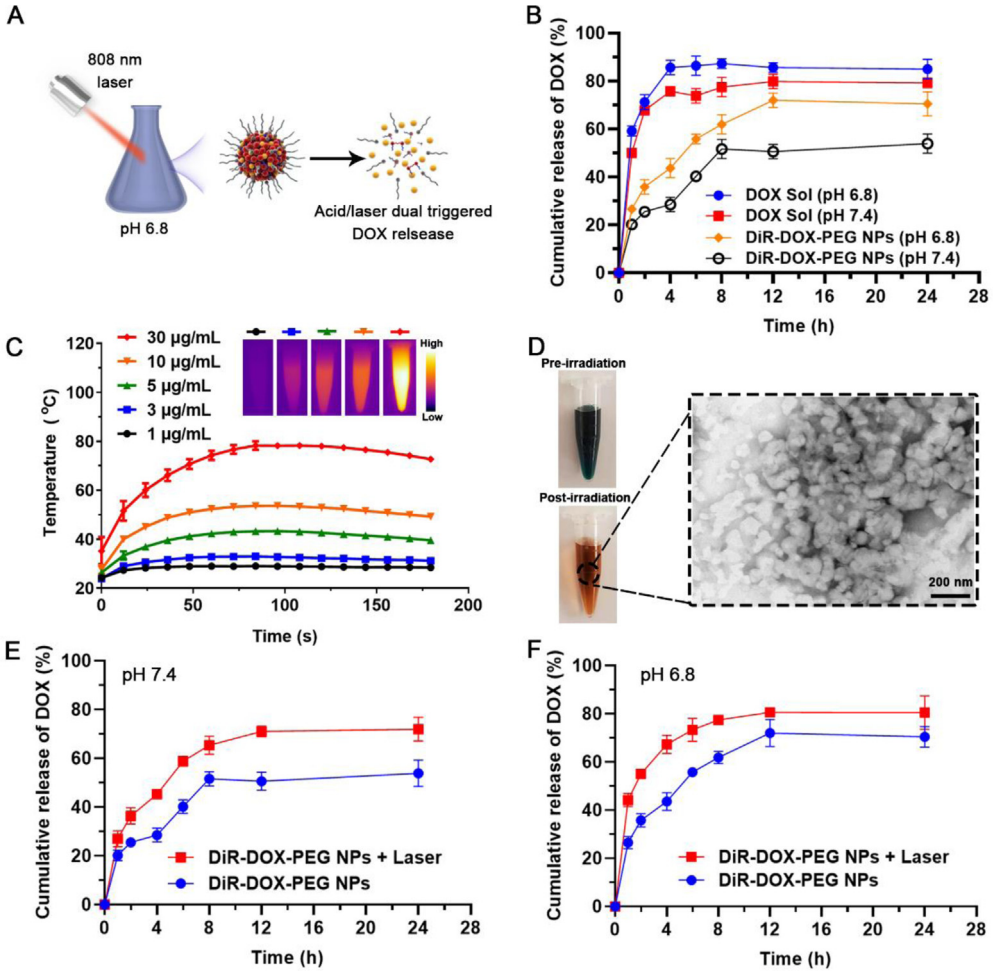

Fig. 3 – Acid and laser dual-triggered drug release. (A) Schematic illustration of the acid and laser dual triggered drug release. (B) Cumulative release curves of DOX in different release media. (C) The temperature change of different concentrations (by the quantities of DiR) of DiR-DOX-PEG NPs under laser irradiation (2 W/cm^2, photos were the thermal image at the maximum temperature). (D) TEM image of DiR-DOX-PEG NPs post-irradiation. (E, F) Cumulative release curves of DOX in different pH with laser irradiation.

obtained and compared. Since the fluorescence emission of DOX and the absorption of DiR were overlapped (Fig. S2), there was a FRET quenched effect (DOX as the donor and DiR as the acceptor) due to the close distance between DOX and DiR molecules in the co-assembled NPs (Fig. 2D). As shown in Fig. 2E and S3, compared with DOX Sol or DiR Sol, the fluorescence of DOX and DiR in the co-assembled NPs was decreased by 60%. Furthermore, the micron aggregate of DiR-DOX-PEG NPs revealed a co-localization of DOX and DiR (Fig. 2F). These results indicated the successful co-assembly of these two drugs. Additionally, DiR-DOX-PEG NPs could keep good stability under the conditions of 4 °C storage for more than one month and in PBS containing 10% serum for more than 24 h (Fig. S4). For long-term storage, DiR-DOX-PEG NPs were lyophilized with 7% sucrose, and the lyophilized samples exhibited good dispersibility with little size change after reconstitution (Fig. 2G).

To further investigate the assembly driving forces of DOX and DiR, a molecular docking simulation was performed. As shown in Fig. 2H, molecular docking results suggested that the long alkyl chain of DiR has significant hydrophobic interaction with the naphthene of DOX (white lines). Besides, strong π-π stacking interaction could be observed between the conjugate rigid plane structure of DiR and DOX (yellow dotted line). The calculated binding energy of DOX and DiR was −7.55 kcal/mol, making it great for co-assembly. Furthermore, DiR-DOX NPs were incubated with NaCl, urea, and SDS solution to verify the intermolecular interactions in the nanoassemblies. As shown in Fig. 2I, DiR-DOX NPs could keep stable in NaCl and urea with little particle size change, while the nanostructure was seriously damaged when incubated with SDS solution. These results were consistent with the simulated results, which also indicated that the assembly of NPs was mainly driven by the hydrophobic interaction between DiR and DOX.

3.2. *pH/laser dual-triggerable drug release*

It was expected that the acid environment would trigger DOX release from DiR-DOX-PEG NPs, and the laser irradiation could also promote this process (Fig. 3A). Thus, the release behaviors

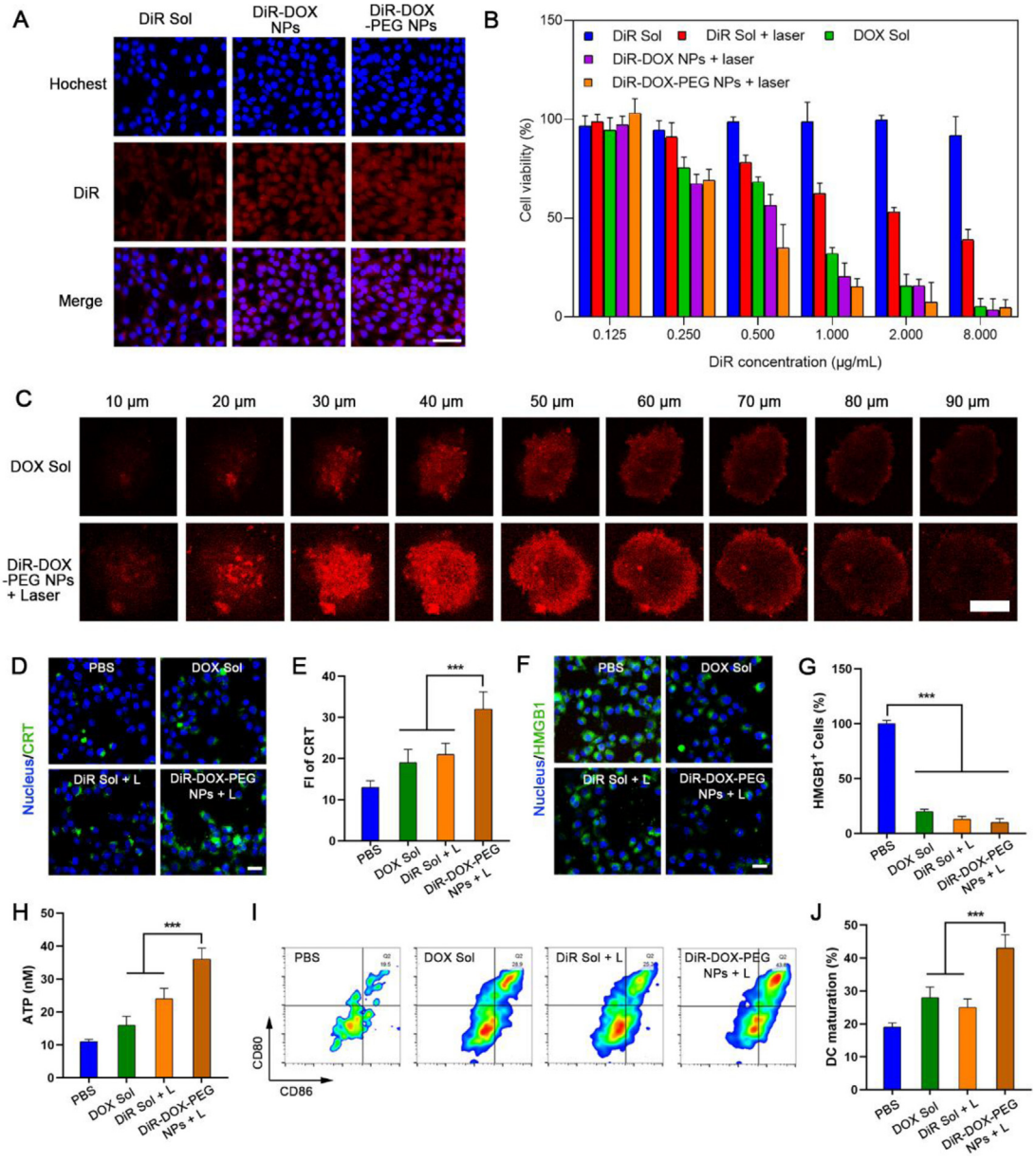

Fig. 4 – Cellular uptake, cytotoxicity and *iv vivo* ICD. (A) CLSM of the uptake of DiR Sol, DiR-DOX NPs, and DiR-DOX-PEG NPs (Scale bar represents 20 μm). (B) Cell viability. (C) CLSM of tumor cell sphere incubated with DOX Sol and DiR-DOX-PEG NPs with laser treatment (Scale bar represents 100 μm). (D) and (E) CLSM and quantitative results of CRT distribution on 4T1 cells (Scale bar represents 10 μm). (F) and (G) CLSM and quantitative results of HMGB1 release from 4T1 after treatment. (H) ATP in culture medium after treatment. (I) Flow cytometric examination and quantitative results of DC maturation by 4T1 cells after treatment.

of co-assembled NPs under an acidic environment and laser irradiation were investigated respectively. As shown in Fig. 3B, the release behaviors of DOX Sol had little difference in pH 6.8 and pH 7.4. By contrast, DOX release from DiR-DOX-PEG NPs significantly increased in the medium (pH 6.8 and 5.0) when compared with the medium (pH 7.4), indicating its pH-sensitive drug release characteristics. The release of DOX from DiR-DOX-PEG NPs was in a pH- and time-dependent manner. The photothermal effect of different concentrations of DiR-DOX-PEG NPs was subsequently evaluated using an infrared thermal image instrument (Fotric 226). As shown in Fig. 3C, the temperature of DiR-DOX-PEG NPs could reach more than 45 °C and keep above 2 min when the concentrations were over 10 μg/ml. The good photothermal effect could not only benefit the tumor cell killing but also help to promote DOX release from the NPs. As shown in Fig. 3D, the structure of DiR-DOX-PEG NPs was greatly changed after laser irradiation. As a result, DOX release rate was significantly increased after laser irradiation in pH 7.4, 6.8 and 5.0 (Fig. 3E-3F and Fig. S5). These results suggested that the release of DOX from DiR-DOX-PEG

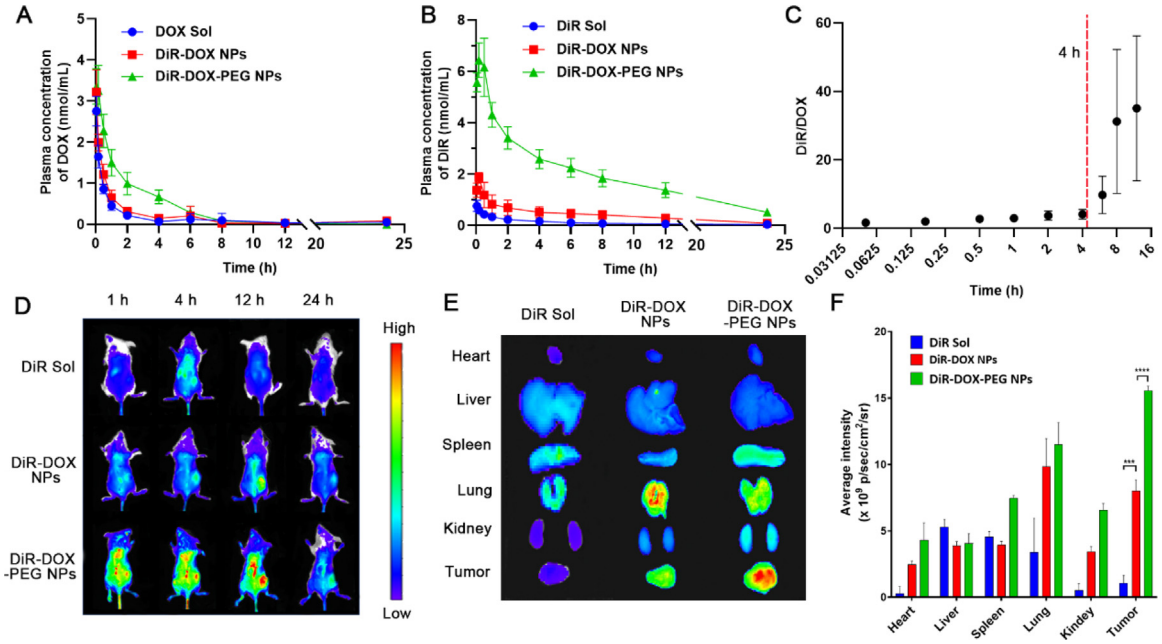

Fig. 5 – Pharmacokinetics and biodistribution ($n = 5$). Plasma concentration changes of (A) DOX and (B) DiR ($n = 6$). (C) Mean molar ratio of DiR/DOX in plasma at different time points. (D) *In vivo* distribution of DiR Sol, DiR-DOX NPs, and DiR-DOX-PEG NPs. (E) *Ex vivo* distribution and (F) the quantitative results of the main organs and tumors at 4 h (DiR Sol) and 12 h (DiR-DOX NPs and DiR-DOX-PEG NPs) post injection.

NPs could be well controlled by laser irradiation, which will benefit to synergistic antitumor effect with good therapeutic security.

3.3. *In vitro synergetic chemo-photothermal therapy and the induced ICD effect*

To investigate the cellular uptake of the co-assemblies and the in *vitro* synergetic chemo-photothermal therapeutic efficiency, 4T1 cells were used for flow cytometry, CLSM analysis, and MTT assay. The fluorescence of DiR was monitored by flow cytometry and CLSM analysis to investigate the time-dependent cellular uptake of co-assemblies. As shown in Fig. S6, DiR-DOX NPs showed similar uptake efficiency with DiR Sol at 0.5 h and slightly increased at 2 h. The cellular uptake of DiR-DOX-PEG NPs was much higher than DiR Sol and DiR-DOX NPs, which could be attributed to the good stability of DiR-DOX-PEG NPs. Moreover, CLSM images also revealed the efficient cellular uptake of DiR-DOX-PEG NPs (Fig. 4A). Notably, although the fluorescence of DiR in the co-assemblies was decreased by 60%, DiR-DOX-PEG NPs still showed much higher cellular uptake efficiency than that of DiR Sol under the same conditions (Fig. 4A). These results suggested that the co-assemblies had distinct advantage over free drug solution in terms of cellular uptake. There is no doubt that high cellular uptake favors the cytotoxicity of NPs. As shown in Fig. 4B and Table S3, compared with DiR Sol and DOX Sol, DiR-DOX NPs significantly inhibited the growth of 4T1 cells under laser irradiation (3 W/cm^2, 5 min). Notably, DiR-DOX-PEG NPs exhibited much stronger cytotoxicity than non-PEGylated NPs, due to their high cellular uptake efficiency.

Furthermore, the high photothermal effect of DiR-DOX-PEG NPs was expected to promote the permeation of DOX into deep tumor tissues. A tumor sphere model was used to investigate the permeation ability of DiR-DOX-PEG NPs. After 4 h incubation and a 5 min laser irradiation (3 W/cm^2, at 2 h post-incubation), the fluorescence signals of DOX in DOX Sol and DiR-DOX-PEG NPs treated tumor sphere were acquired. As shown in Fig. 4C, DiR-DOX-PEG NPs treated tumor sphere exhibited a much stronger fluorescence signal from 20 to 80 μm than that of DOX Sol treated tumor sphere. The enhanced tissue permeation ability should be attributed to the increased tissue space induced by the photothermal effect of DiR-DOX-PEG NPs.

To identify the ICD induced by DiR-DOX-PEG NPs, the main biomarkers including CRT, HMGB1 and ATP were monitored after the treatment. As shown in Fig. 4D and 4E, after DOX or DiR treatment, the CRT (acting as the “eat me” signal) was significantly exposed to the surface of the cells. Compared with DOX and DiR treatment, the DOX-DiR-PEG NPs treatment triggered much more CRT exposure, which might recruit immune cells to process and present tumor antigen in the *in vivo* treatment. Moreover, the HMGB1 and ATP (acting as the damage-associated signals) were released more to the culture medium which could efficiently stimulate the maturation of antigen presenting cells (Fig. 4F-4H). The immune activity assay showed that DiR-DOX-PEG NPs treatment induced ICD stimulated around 43% mutation of BMDCs compared with the single treatment of DOX (28%) and DiR(25%) (Fig. 4I-

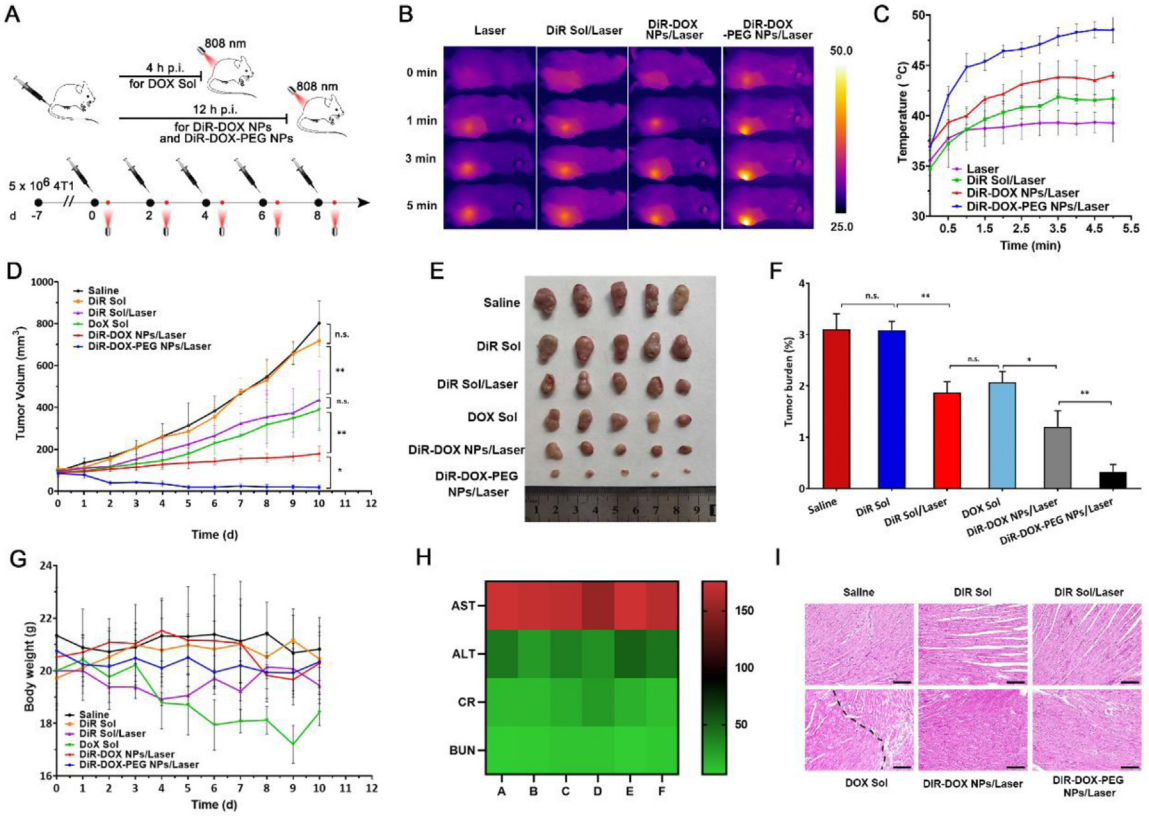

Fig. 6 – *In vivo* photothermal effect and anti-tumor therapy. (A) Therapeutic protocol. (B) Photothermal images of mice under laser irradiation at 4 h (DiR Sol, DiR-DOX NPs) and 12 h (DiR-DOX-PEG NPs) post injection. (C) Temperature change during the irradiation ($n = 3$). (D) Tumor growth curves ($n = 5$). (E) Photos of the ex vivo tumors after the treatment. (F) Tumor burden. (G) Body weight change. (H) Hepatorenal function parameters ($n = 3$). (ALT: alanine aminotransferase; AST: aspartate aminotransferase; BUN: blood urea nitrogen; CRE: creatinine. A: Saline; B: DiR Sol; C: DiR Sol/laser; D: DOX Sol; E: DiR-DOX NPs/laser; F: DiR-DOX-PEG NPs/laser) (I) H&E staining of the heart tissue. (Damaged tissues were marked by the dotted line).

4J). The strong ICD effect of DiR-DOX-PEG NPs treatment exhibited the potential for immune activation against tumors *in vivo*.

3.4. *Pharmacokinetics and biodistribution*

The pharmacokinetic behaviors of the co-assembled NPs were investigated in SD rats. As shown in Fig. 5A-5B and Table S4, DiR Sol and DOX Sol were quickly cleared from the blood circulation. However, although the non-PEGylated NPs (DiR-DOX NPs) improved the pharmacokinetic behaviors of the drugs to some extent, they were also quickly cleared from the blood. In contrast, the circulation time of DOX and DiR in the PEGylated NPs (DiR-DOX-PEG NPs) was significantly prolonged, indicating the distinct advantage of the PEGylated co-assemblies. Furthermore, the plasma molar ratio of DiR/DOX could maintain a constant ratio at 2:1 (the optimum synergy ratio) after injection for 4 h (Fig. 5C). Moreover, both of them had a very similar blood half-life (Table S4). These results revealed that the PEGylated NPs could remain stable as intact particles in the circulation after intravenous injection. It's reasonable for free drugs to be quickly cleared from the body due to their short half-time. Additionally, the poor pharmacokinetic behavior of DiR-DOX NPs should be attributed to their hydrophobic surface and inferior colloidal stability (Fig. S3).

The *in vivo* and *ex vivo* distribution of DiR-DOX-PEG NPs were investigated on 4T1 tumor-bearing mice by monitoring the fluorescence changes of DiR. As shown in Fig. 5D, DiR Sol reached the maximum accumulation in the tumor tissues at 4 h post injection. Subsequently, the fluorescence signals gradually decreased. DiR-DOX NPs and DiR-DOX-PEG NPs were continuously accumulated into the tumor tissue post injection and reached the maximum accumulation at 12 h. Moreover, the overall fluorescence intensity of DiR-DOX-PEG NPs in animals was much stronger than that of DiR Sol and DiR-DOX NPs, which was consistent with the pharmacokinetics results. To further confirm the results, the *ex vivo* distribution of the above formulations in the main organs and tumors was explored at their maximum accumulation time points (DiR Sol at 4 h, DiR-DOX NPs, and DiR-DOX-PEG NPs at 12 h). As shown in Fig. 5E and 5F, the accumulation of DiR-DOX NPs in tumor tissue was higher than DiR Sol, probably due to its better pharmacokinetic behavior

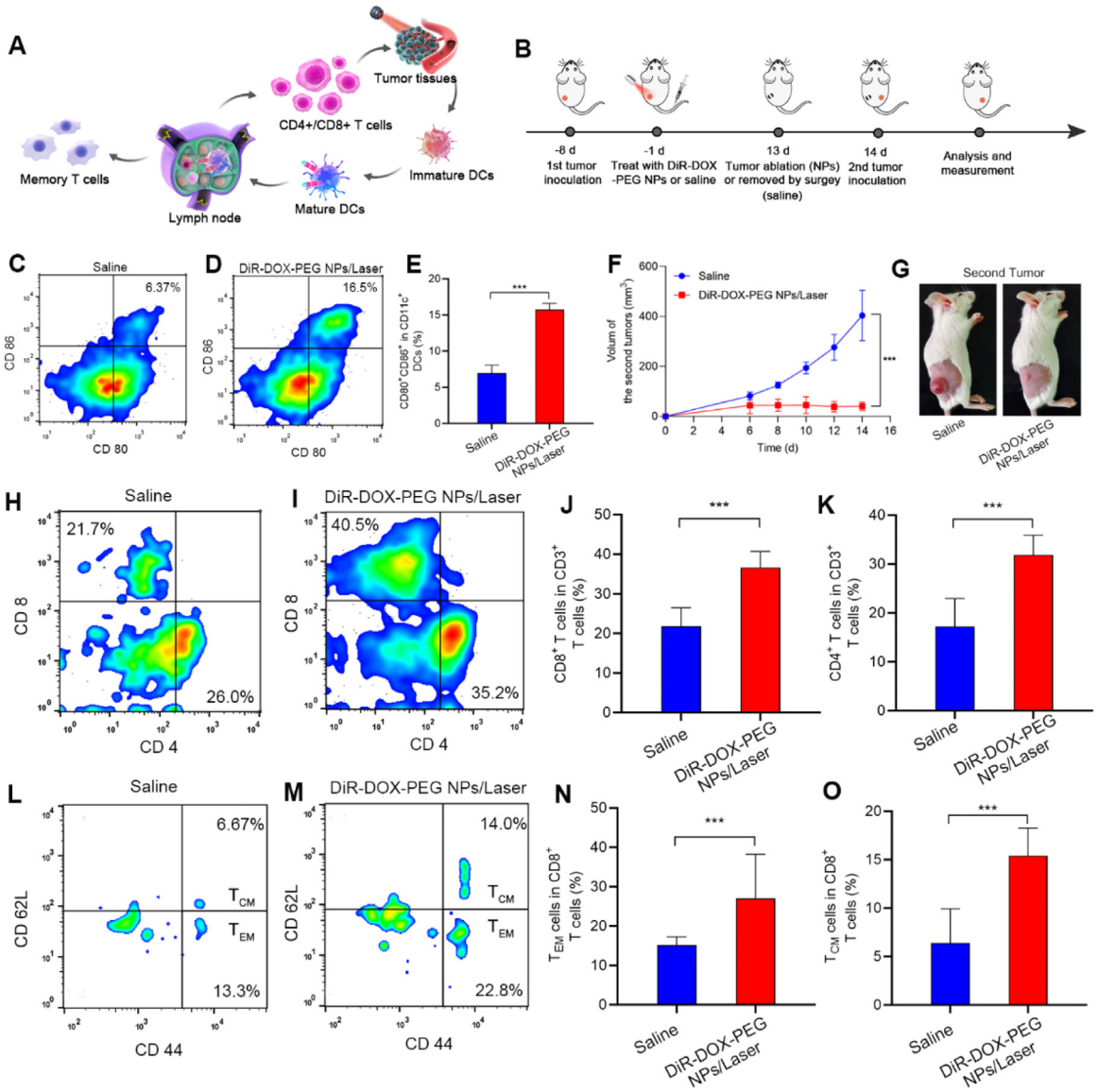

Fig. 7 – Immune activation and preventing tumor recurrence. (A) Schematic illustration of the immune activation *in vivo*. (B) Therapeutic and testing protocol. (C-E) Represent results and the quantitative results for the flow cytometric analysis of the maturation DCs ($CD80^+/CD86^+$ in $CD11c^+$ cells) in draining lymph nodes of the mice after different treatments. (F) Tumor volume change of the second tumors. (G) Represents photos of the second tumor after 14 d of inoculation. (H-K) Represent results and the quantitative results of the flow cytometric analysis of the $CD4^+/CD8^+$ T cells ($CD4^+/CD8^+$ T cells in $CD3^+$ cells) in mice peripheral blood after 14 d second tumor inoculations. (L-O) Represent results and the quantitative results of the flow cytometric analysis of the memory $CD8^+$ T cells ($CD44^+/CD62L$ T cells in $CD8^+$ cells) in mice peripheral blood after 14 d second tumor inoculations.

(Fig. 5B). Notably, the DiR-DOX-PEG NPs displayed the highest tumor-specific distribution, even higher than that in main organs. The efficient tumor distribution of DiR-DOX-PEG NPs could be mainly ascribed to their long circulation and the EPR effect.

3.5. *In vivo photothermal effect and synergetic chemo-photothermal therapy*

The *in vivo* photothermal effects were investigated on 4T1 tumor-bearing mice. According to the biodistribution results (Fig. 5D), the mice receiving DiR Sol were irradiated at 4 h post injection, and the groups of DiR-DOX NPs/DiR-DOX-PEG NPs were irradiated at 12 h post injection (Fig. 6A). As shown in Fig. 6B-6C, the local temperature in the tumors in DiR Sol-treated mice did not change much, while the tumor-local temperature of DiR-DOX NPs-injected mice could reach an effective therapeutic range (> 42 °C). Notably, the tumor-local temperature of the mice receiving DiR-DOX-PEG sharply increased, exceeding 45 °C and maintaining for more than 3 min. The excellent was caused by the long circulation and high accumulation (Fig. 5).

The highly efficient photothermal efficiency of the co-assemblies encouraged us to further investigate the *in vivo* antitumor effect. Therefore, thirty 4T1 tumor-bearing mice (tumor volumes were around 100 mm^3) were randomly divided into six groups and separately injected with Saline, DiR Sol, DOX Sol, DiR-DOX NPs, and DiR-DOX-PEG NPs for each group (DiR: 5.0 mg/kg, DOX: 1.35 mg/kg). After different time intervals (Fig. 6A), DiR Sol, DiR-DOX NPs, and DiR-DOX-PEG NPs were irradiated with an 808 nm laser (2 W/cm^2) for PTT [40,41]. The mice were treated every two days. After five treatments, the mice were killed, and the main organs, as well as tumors and serum samples, were collected (Fig. 6A). As shown in Fig. 6D, the tumor volume of mice treated with DiR Sol increased nearly as fast as the saline control. The chemotherapy of DOX or PTT of DiR could inhibit tumor growth to a certain extent, but the tumor volume progressed very largely eventually. By contrast, the synergetic chemo-photothermal therapy of DiR-DOX NPs significantly inhibits tumor growth, and the tumor volumes hardly changed during the treatment period. The efficient tumor inhibition could attribute to the synergetic chemo-photothermal therapy, as the photothermal effect could promote the deep penetration of DOX (Fig. 4C). As expected, the DiR-DOX-PEG NPs had the best tumor inhibition effect with the tumor nearly disappearing (Fig. 6E). Compared with DiR-DOX NPs, the enhanced antitumor efficiency of DiR-DOX-PEG NPs could be attributed to the long blood circulation and efficient photothermal effect of DiR-DOX-PEG NPs (Fig. 5, 6B and 6C). The tumor burden rate also revealed the good anti-tumor effect of DiR-DOX-PEG NPs (Fig. 6F). Moreover, there was no apparent toxicity found in the liver, spleen, lung, and kidney after treatments with DiR-DOX-PEG NPs (Fig. 6H and S7). Notably, DOX Sol showed certain toxicity to the heart tissue (Fig. 6I), and the body weight decreased during the treatment (Fig. 6G). These results indicated that the co-assembly strategy could markedly improve the safety of chemotherapeutic agents (*e.g.*, DOX).

3.6. *Immune activation and tumor recurrence prevention*

It has been reported that both the DOX-mediated chemotherapy and PDT could boost the immune system, promote the maturation of dendritic cells to present tumor antigen to T cells, and cause specific tumor killing [14,31]. More importantly, memory T cells could be generated against tumor recurrence during this process (Fig. 7A). Based on this rationale, the potent anti-cancer efficiency of DiR-DOX-PEG NPs encouraged us to further evaluate its tumor recurrence prevention effect. Several typical immunological indicators were monitored after the treatment of DiR-DOX-PEG NPs and saline. Furthermore, a tumor recurrence prevention experiment was carried out. Firstly, twenty tumor-bearing mice were established and the mice experienced the entire five times therapy of DiR-DOX-PEG NPs or saline (Fig. 7B). The tumor-draining lymph nodes of half of the mice were collected and DCs were analyzed by FACS (Fig. 7C-7E), the amount of mature DCs in DiR-DOX-PEG NPs treated mice are much higher compared with saline-treated mice, which indicated its strong immune-stimulating effect. The strong immune activation might be induced from the ICD during the DiR-DOX-PEG NPs treatment, as the main biomarker, CRT, was significantly up-regulated after the treatment (Fig. S8). Subsequently, the mice were rechallenged with the 4T1 tumor model. 5×10^6 4T1 tumors were inoculated on the different sides of the flank and the tumor volumes were recorded (Fig. 7B).

As shown in Fig. 7F-7G, the tumors grew rapidly in the saline-treated group, while the tumors barely progressed in the DiR-DOX-PEG NPs treated group. The efficient tumor recurrence prevention of DiR-DOX-PEG NPs was probably due to the immune activation during the treatment process. The mice were sacrificed 14 d after the second tumor inoculation and the peripheral blood lymphocytes were analyzed. As shown in Fig. 7H-7K, the mice treated with DiR-DOX-PEG NPs showed significantly upregulated $CD4^+/CD8^+$ T cells, which could efficiently kill tumor cells. Combined with analysis of previous ICD-inducing factor detection and high expression of cytotoxic T lymphocytes cells ($CD4^+/CD8^+$) in tumor tissue, it demonstrated DiR-DOX-PEG NPs-mediated tumor therapy successfully induced ICD and activated immune response. In order to further evaluate its immune memory function, we detected central or environmental memory $CD8^+$T cells (T_{CM}/T_{EM}). Generally, T_{CM} and T_{EM} can produce effector T cells or cytokines, respectively, to exert immune effect when they are again exposed to antigenic stimuli. As a result, much higher amounts of T_{CM} and T_{EM} were found in the DiR-DOX-PEG NPs treated mice compared with saline-treated mice (Fig. 7L-7O), indicating the excellent ability to activate long-term immune memory against tumor recurrence.

4. Conclusions

In this study, facile fabrication of carrier-free pure drug co-assembled nanosystem of DiR and DOX was reported for immune-activating chemo-photothermal therapy. We found that DOX and DiR could co-assemble into uniform nanoparticles in water, which was driven by the hydrophobic interaction of the alkyl chain and the π-π stacking interaction between the conjugated structure of two kinds of molecules. DOX release could be triggered by the acidic environment and the destruction of DiR under laser irradiation. After PEG modification, the co-assembled nanoparticles could significantly extend the systemic circulation time and increase the accumulation of tumor sites. After the combination of chemo-photothermal therapy, the tumor growth was significantly inhibited with the tumor nearly disappeared. More interestingly, the mice were found to acquire immune memory against tumor recurrence after treatment with the nanoassembly. Such a pure drug co-assembled nanosystem with ingenious fabrication, controllable release as well as immune activation capacity shows great potential to provide a co-delivery platform for small-molecule drug-based chemo-photo-immunotherapy.

Conflicts of interest

The authors declare no interest in this paper.

Acknowledgments

This work was financially supported by the Liaoning Revitalization Talents Program (no. XLYC1907129), the National Natural Science Foundation of China (no. 82161138029), the Excellent Youth Science Foundation of Liaoning Province (no. 2020-YQ-06), and the China Postdoctoral Science Foundation (no. 2020M670794 and no. 2021MD703858).

Supplementary materials

Supplementary material associated with this article can be found, in the online version, at doi:10.1016/j.ajps.2022.02.004.

REFERENCES

[1] Wang K, Ye H, Zhang X, Wang X, Yang B, Luo C, et al. An exosome-like programmable-bioactivating paclitaxel prodrug nanoplatform for enhanced breast cancer metastasis inhibition. Biomaterials 2020;257:120224.
[2] Zhang J, Nie W, Chen R, Chelora J, Wan Y, Cui X, et al. Green mass production of pure nanodrugs via an ice-template-assisted strategy. Nano Lett 2019;19:658–65.
[3] Yu W, Shevtsov M, Chen X, Gao H. Advances in aggregatable nanoparticles for tumor-targeted drug delivery. Chin. Chem Lett 2020;31:1366–74.
[4] Zheng L, Hu X, Wu H, Mo L, Xie S, Li J, et al. *In vivo* monocyte/macrophage-hitchhiked intratumoral accumulation of nanomedicines for enhanced tumor therapy. J Am Chem Soc 2020;142:382–91.
[5] Li S, Shan X, Wang Y, Chen Q, Sun J, He Z, et al. Dimeric prodrug-based nanomedicines for cancer therapy. J Control Release 2020;326:510–22.
[6] Chen Q, Liu G, Liu S, Su H, Wang Y, Li J, et al. Remodeling the tumor microenvironment with emerging nanotherapeutics. Trends Pharmacol Sci 2018;39:59–74.
[7] Wang Y, Wang X, Zhang J, Wang L, Ou C, Shu Y, et al. Gambogic acid-encapsulated polymeric micelles improved therapeutic effects on pancreatic cancer. Chin Chem Lett 2019;30:885–8.
[8] Zhang A, Hai L, Wang T, Cheng H, Li M, He X, et al. Nir-triggered drug delivery system based on phospholipid coated ordered mesoporous carbon for synergistic chemo-photothermal therapy of cancer cells. Chin Chem Lett 2020;31:3158–62.
[9] Wang Y, Li S, Wang X, Chen Q, He Z, Luo C, et al. Smart transformable nanomedicines for cancer therapy. Biomaterials 2021:120737.
[10] Maman S, Witz IP. A history of exploring cancer in context. Nat Rev Cancer 2018;18:359–76.
[11] Luo C, Sun J, Sun B, He Z. Prodrug-based nanoparticulate drug delivery strategies for cancer therapy. Trends Pharmacol Sci 2014;35:556–66.
[12] Luo C, Sun J, Sun B, Liu D, Miao L, Goodwin TJ, et al. Facile fabrication of tumor redox-sensitive nanoassemblies of small-molecule oleate prodrug as potent chemotherapeutic nanomedicine. Small 2016;12:6353–62.
[13] Sun B, Luo C, Zhang X, Guo M, Sun M, Yu H, et al. Probing the impact of sulfur/selenium/carbon linkages on prodrug nanoassemblies for cancer therapy. Nat Commun 2019;10:3211.
[14] Feng B, Niu Z, Hou B, Zhou L, Li Y, Yu H. Enhancing triple negative breast cancer immunotherapy by icg-templated self-assembly of paclitaxel nanoparticles. Adv Funct Mater 2019;30:1906605.
[15] Zhang X, Li N, Zhang S, Sun B, Chen Q, He Z, et al. Emerging carrier-free nanosystems based on molecular self-assembly of pure drugs for cancer therapy. Med Res Rev 2020;40:1754–75.
[16] Zhang X, Xiong J, Wang K, Yu H, Sun B, Ye H, et al. Erythrocyte membrane-camouflaged carrier-free nanoassembly of fret photosensitizer pairs with high therapeutic efficiency and high security for programmed cancer synergistic phototherapy. Bioact Mater 2021;6:2291–302.
[17] Wang Y, Luo C, Zhou S, Wang X, Zhang X, Li S, et al. Investigating the crucial roles of aliphatic tails in disulfide bond-linked docetaxel prodrug nanoassemblies. Asian J Pharma Sci 2021.
[18] Zhang X, Sun B, Zuo S, Chen Q, Gao Y, Zhao H, et al. Self-assembly of a pure photosensitizer as a versatile theragnostic nanoplatform for imaging-guided antitumor photothermal therapy. ACS Appl Mater Interfaces 2018;10:30155–62.
[19] Li Y, Liu G, Ma J, Lin J, Lin H, Su G, et al. Chemotherapeutic drug-photothermal agent co-self-assembling nanoparticles for near-infrared fluorescence and photoacoustic dual-modal imaging-guided chemo-photothermal synergistic therapy. J Control Release 2017;258:95–107.
[20] Mei H, Cai S, Huang D, Gao H, Cao J, He B. Carrier-free nanodrugs with efficient drug delivery and release for cancer therapy: from intrinsic physicochemical properties to external modification. Bioact Mater 2022;8:220–40.
[21] Zhang S, Wang Y, Kong Z, Zhang X, Sun B, Yu H, et al. Pure photosensitizer-driven nanoassembly with core-matched pegylation for imaging-guided photodynamic therapy. Acta Pharmaceutica Sinica B 2021;11:3636–47.
[22] Zhang S, Wang Z, Kong Z, Wang Y, Zhang X, Sun B, et al. Photosensitizer-driven nanoassemblies of homodimeric prodrug for self-enhancing activation and synergistic chemo-photodynamic therapy. Theranostics 2021;11:6019.
[23] Wang D, Niu L, Qiao ZY, Cheng DB, Wang J, Zhong Y, et al. Synthesis of self-assembled porphyrin nanoparticle photosensitizers. ACS Nano 2018;12:3796–803.
[24] Zhang R, Zhu Z, Lv H, Li F, Sun S, Li J, et al. Immune checkpoint blockade mediated by a small-molecule nanoinhibitor targeting the pd-1/pd-l1 pathway synergizes with photodynamic therapy to elicit antitumor immunity and antimetastatic effects on breast cancer. Small 2019;15:e1903881.
[25] Medicine USNLO Trial of nanopac?in subjects with locally advanced pancreatic adenocarcinoma [Online]. https://clinicaltrials.gov/ct2/show/NCT03077685?term=nanopac.
[26] Melero I, Berman DM, Aznar MA, Korman AJ, Perez Gracia JL, Haanen J. Evolving synergistic combinations of targeted immunotherapies to combat cancer. Nat Rev Cancer 2015;15:457–72.
[27] Xu J, Lv J, Zhuang Q, Yang Z, Cao Z, Xu L, et al. A general strategy towards personalized nanovaccines based on fluoropolymers for post-surgical cancer immunotherapy. Nat Nanotechnol 2020;15:1043–52.
[28] Li AW, Sobral MC, Badrinath S, Choi Y, Graveline A, Stafford AG, et al. A facile approach to enhance antigen response for personalized cancer vaccination. Nat Mater 2018;17:528–34.
[29] Siegel RL, Miller KD, Fuchs HE, Jemal A. Cancer statistics, 2021. CA Cancer J Clin 2021;71:7–33.
[30] Siegel RL, Miller KD, Jemal A. Cancer statistics, 2020. CA Cancer J Clin 2020;70:7–30.

[31] Yu Z, Guo J, Hu M, Gao Y, Huang L. Icaritin exacerbates mitophagy and synergizes with doxorubicin to induce immunogenic cell death in hepatocellular carcinoma. ACS Nano 2020;14:4816–28.
[32] Fan Z, Liu H, Xue Y, Lin J, Fu Y, Xia Z, et al. Reversing cold tumors to hot: an immunoadjuvant-functionalized metal-organic framework for multimodal imaging-guided synergistic photo-immunotherapy. Bioact Mater 2021;6:312–25.
[33] Ding K, Zheng C, Sun L, Liu X, Yin Y, Wang L. Nir light-induced tumor phototherapy using icg delivery system based on platelet-membrane-camouflaged hollow bismuth selenide nanoparticles. Chin Chem Lett 2020;31:1168–72.
[34] Deng Z, Jiang C, Younis MR, Lei S, He Y, Zheng H, et al. Mild hyperthermia-enhanced chemo-photothermal synergistic therapy using doxorubicin-loaded gold nanovesicles. Chin Chem Lett 2021;32:2411–14.
[35] Chen Y, Jiang M, Xiong L, Yao X, Fan M, Chen D, et al. Novel photo-theranostic gdb6 nanoparticles for fluorescence imaging and nir-photothermal therapy. Chin Chem Lett 2021;32:3487–90.
[36] Ng CW, Li J, Pu K. Recent progresses in phototherapy-synergized cancer immunotherapy. Adv Funct Mater 2018;28:1804688.
[37] Zhang W, Wang F, Hu C, Zhou Y, Gao H, Hu J. The progress and perspective of nanoparticle-enabled tumor metastasis treatment. Acta Pharmaceutica Sinica B 2020;10:2037–53.
[38] Peng S, Xiao F, Chen M, Gao H. Tumor-microenvironment-responsive nanomedicine for enhanced cancer immunotherapy. Adv Sci (Weinh) 2022;9:e2103836.
[39] Zhang J, Shen L, Li X, Song W, Liu Y, Huang L. Nanoformulated codelivery of quercetin and alantolactone promotes an antitumor response through synergistic immunogenic cell death for microsatellite-stable colorectal cancer. ACS Nano 2019;13:12511–24.
[40] He X, Bao X, Cao H, Zhang Z, Yin Q, Gu W, et al. Tumor-penetrating nanotherapeutics loading a near-infrared probe inhibit growth and metastasis of breast cancer. Adv Funct Mater 2015;25:2831–9.
[41] Zhao Z, Zhang X, Zhang H, Shan X, Bai M, Wang Z, et al. Elaborately engineering a self-indicating dual-drug nanoassembly for site-specific photothermal-potentiated thrombus penetration and thrombolysis. Adv Sci 2021:2104264.